Research Article Vol. 4, No. 11 / November 2017 / Optica 1373

3D image scanning microscopy with engineered excitation and detection

Clemens Roider,[1] Rafael Piestun,[2] and Alexander Jesacher[1,*]

[1]Division of Biomedical Physics, Innsbruck Medical University, Müllerstraß e 44, 6020 Innsbruck, Austria
[2]Department of Electrical and Computer Engineering, University of Colorado, Boulder, Colorado 80309, USA
*Corresponding author: alexander.jesacher@i-med.ac.at

Received 31 July 2017; revised 28 September 2017; accepted 10 October 2017 (Doc. ID 300465); published 7 November 2017

Scanning microscopes are important research tools for investigating 3D specimens. Modern beam shaping techniques can be combined with suitably designed data processing algorithms to improve instrument versatility and imaging performance. Here we introduce image scanning microscopy with freely programmable excitation and detection pupils and investigate point spread function (PSF) designs for parallel 3D information acquisition. The volumetric data is collected in a single 2D scan without the requirement of physical refocus. By sculpturing the excitation and detection PSFs into helical shapes of opposing handedness, we are able to capture sample information in a volume whose axial extension measures more than four times the z resolution. In a more generalized approach, jointly optimized phase masks are used in both pupils to shape the PSFs. As an exemplary case, we study the use of beam-splitting phase masks for the parallel scanning in multiple planes. The image reconstruction algorithm optimally integrates this information according to the various signal-to-noise ratios. Generalized PSF engineering scanning systems provide resolution improvement relative to confocal microscopy while accelerating data collection. We analyze the opportunities, trade-offs, and limitations of the approach.

OCIS codes: (170.6900) Three-dimensional microscopy; (180.5810) Scanning microscopy; (050.1970) Diffractive optics; (070.6120) Spatial light modulators.

https://doi.org/10.1364/OPTICA.4.001373

1. INTRODUCTION

Point spread function (PSF) engineering refers to the optimization of the optical transfer function of an imaging system towards a specific task in conjunction with detectors and possible reconstruction algorithms. Many applications aim at improving the spatial resolution, with stimulated emission depletion (STED) microscopy representing a well-known example [1]. PSF engineering is also used in linear imaging systems, for instance, to achieve a "Toraldo-type" resolution increase [2–4], to increase the axial localization accuracy in single molecule localization [5,6], or to increase the depth of field [7–10].

In confocal microscopy, excitation and detection PSFs are equally important for image formation, which is why shaping both PSFs can be advantageous. Indeed, the use of resolution-enhancing filters in the excitation and detection pupils has already been discussed [3,11–13]. In a recent paper, the construction of color-dependent PSFs has been demonstrated, where the Stokes shift of the fluorescence light was exploited to obtain different PSFs on the excitation and emission sides [14].

Lately, the practical implementation of image scanning microscopy (ISM) [15,16] has opened an interesting opportunity for PSF engineering. Here, the pinhole and large area detector are replaced by a pixelated detector taking images at every scanpoint. This means that the system has the capability of collecting much more information from the sample than a classical confocal system. Information contained in the change of the PSF shape is detected rather than being "cut off" by a pinhole.

Here we present generalized pupil phase engineering for ISM in the sense that both excitation and detection PSFs are manipulated. This general system shall be further denoted as "engineered ISM (eISM)." We investigate two specific approaches that support 3D imaging in eISM: the first employs helical excitation and detection PSFs and is therefore further referred to as *helix-helix imaging*. This approach can be thought of as an advancement of the recent 3D imaging method called RESCH (Refocusing after Scanning using Helical phase engineering) [17]. The second implementation uses beam-splitting phase masks in the excitation and detection pupils to produce specifically designed focus arrangements. Both methods are compared in view of 3D imaging capabilities, spatial resolution, and photon efficiency. We present results from numerical simulations and imaging experiments carried out with fluorescent microbeads and fixed, fluorescently labeled COS-7 cells.

The paper is organized as follows. In Section 2 we introduce the microscope setup and a mathematical model of the image formation, which helps explain the considerations in choosing specific PSF shapes. The image construction process is briefly reviewed in Section 3. In Sections 4 and 5, the imaging properties

Corrected 15 November 2017

of the helix-helix system and the beam-splitting system are investigated by means of numerical simulations. Finally, Section 5 presents experimental results from imaging microbeads and fixed cells obtained with both approaches.

2. SETUP AND IMAGE FORMATION

The basic light path is sketched in the inset of Fig. 1. The excitation laser is coupled into the objective lens and generates fluorescence in the object, which is collected by the same objective lens, and finally imaged into the camera plane by the tube lens. It is important to understand that every detector pixel m of the camera can be regarded as an individual confocal detector, acquiring an individual confocal image I_m when a scan is performed. Thus, if a single scanpoint image consists of M pixels, the raw data of an entire scan consists of M confocal images I_m.

A sketch of the microscope is shown in Fig. 1. It is a point-scanning epi-detection microscope that uses galvanometric mirrors to sweep the focus over the sample. A single spatial light modulator (SLM) is used to display phase masks for sculpturing excitation and detection PSFs. The SLM is reflective but shown as a transmissive device for the sake of clarity. An important difference to a standard confocal microscope is that our system employs a sCMOS camera (Hamamatsu ORCA-Flash4.0 V2) instead of a physical pinhole in conjunction with a single bucket detector (e.g., a photomultiplier tube). At every scanpoint, a small image of the proximal region around the excitation focus is taken. Such an image is further denoted as "scanpoint image."

In the following, we take two steps to formulate the image formation in eISM. In the first step we describe the formation of a scanpoint image in the detector plane. Based on this result, we then derive the confocal images I_m collected by the detector pixels m in the course of a scan and their respective imaging PSFs h_m. The process of combining the images I_m to form the final image of the object is explained in Section 3.

3D imaging can be described via 3D Fourier transforms, provided the regions in the object space are sufficiently close to the focal point [18]. This model is valid for high numerical apertures and compatible to the vectorial nature of electric fields, although we shall consider scalar and single frequency fields (i.e., no Stokes shift) in this section for the sake of simplicity. We would like to note, however, that the numerical simulations following later in this paper consider polarization and Stokes shift as long as not stated otherwise.

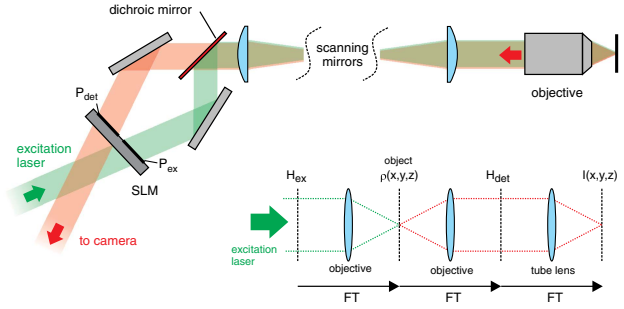

Fig. 1. Sketch of the eISM microscope. A single LCoS SLM (here shown as transmissive device for clarity) is used to display individual diffractive patterns (P_{ex} and P_{det}) for shaping the excitation and detection PSFs independently. The inset in the lower right corner shows the light path unfolded to visualize the image formation described in Eq. (1). H_{ex} and H_{det} are the excitation and detection optical transfer functions, respectively, and ρ is the fluorophore density of the object. The abbreviation "FT" denotes the optical Fourier transform performed by a lens.

The formation of a scanpoint image (which is a wide-field image) on the camera can be mathematically described as follows:

$$\begin{aligned} I_{\mathrm{WF}}(\vec{x}) &\propto \mathcal{F}\{\mathcal{F}\{\mathcal{F}\{H_{\mathrm{ex}}(\vec{k})\}\cdot\rho(\vec{x})\}\cdot H_{\mathrm{det}}(\vec{k})\} \\ &= [(h_{\mathrm{ex}}\cdot\rho)\star h_{\mathrm{det}}](\vec{x}). \end{aligned} \tag{1}$$

In this equation, $\mathcal{F}$ denotes the optical 3D Fourier transform, and $\vec{x}$ and $\vec{k}$ are the 3D coordinate vectors in the object/camera and pupil planes. H_{ex} and H_{det} are the optical transfer functions on the excitation and detection side, and their Fourier transforms are the respective intensity PSFs h_{ex} and h_{det}. $I_{\mathrm{WF}}(\vec{x})$ is the 3D intensity distribution in the image space, whose $x-y$ section at $z=0$ is the scanpoint image captured by the camera: $I_{\mathrm{cam}}(x,y)=I_{\mathrm{WF}}(x,y,0)$. The fluorophore density of the object is described by $\rho(\vec{x})$. The symbol $*$ denotes the 3D convolution operator and $\star$ the 3D cross-correlation. Note that the inversion of all three axes (x, y, z) by the first two subsequent 3D Fourier transforms is consistent with our epi-detection geometry, where the z axis is likewise inverted.

In ISM, every pixel m of the detector has its individual PSF h_m, which is determined by the excitation and detection PSFs h_{ex} and h_{det} as well as the shape of the pixel, $P_m=\mathrm{rect}((x-x_m)/p, (y-y_m)/p)$, where rect is the 2D rectangular function, p the side length of a detector pixel, and x_m, y_m the center coordinates of pixel m. Starting from the epi-fluorescence wide-field image formation [Eq. (1)], we can calculate the intensity of the confocal image I_m at scanpoint (x_s, y_s) by multiplying the respective scanpoint image $I_{\mathrm{cam}}(x,y,x_s,y_s)$ with the pixel function $P_m(x,y)$ and integrating over the entire camera plane:

$$\begin{aligned} I_m(x_s,y_s) &\propto \iint \mathrm{d}x\mathrm{d}y P_m(x,y)\Bigg\{\iiint \mathrm{d}\hat{x}\mathrm{d}\hat{y}\mathrm{d}\hat{z}h_{ex}(\hat{x},\hat{y},\hat{z}) \\ &\quad\cdot\rho(\hat{x}-x_s,\hat{y}-y_s,\hat{z})h_{\mathrm{det}}(x+\hat{x},y+\hat{y},\hat{z})\Bigg\} \\ &= (\rho * h_m)(x_s,y_s,0), \end{aligned} \tag{2}$$

where the total PSFs h_m can be identified to be

$$h_m(\hat{x},\hat{y},\hat{z}) = h_{\mathrm{ex}}(\hat{x},\hat{y},\hat{z})(P_m \star_{2D} h_{\mathrm{det}})(\hat{x},\hat{y},\hat{z}). \tag{3}$$

3. IMAGE CONSTRUCTION IN EISM

In regular ISM, h_{ex} and h_{det} can be assumed Gaussian. Therefore, the pixel-dependent PSFs h_m are likewise approximately Gaussian and differ only by their strengths and lateral shifts, which depend on the pixel positions (x_m, y_m). Thus, a straightforward method for constructing the final image is to compensate for these shifts followed by adding up all images I_m [15,19], a procedure which has become known as "pixel reassignment."

For general PSF shapes, however, pixel reassignment is no longer suitable, and alternative ways of data processing must be employed. One possibility is to use concepts of parameter estimation from multiple measurements [20,21]. In microscopy, these multiple measurements represent multiple "views" of the specimen, which is why such algorithms are often denoted as "multi-view (MV)" or "joint" deconvolution algorithms. Also, ISM can be considered a multi-view instrument because every detector pixel delivers an individual view of the specimen, characterized by its individual PSF h_m.

Maximum-likelihood estimation of the object from multiple measurements has been demonstrated for various imaging modalities, such as emission tomography [22], multi-angle tomographic confocal microscopy [23], programmable array microscopy (PAM) [24], selective plane illumination microscopy (SPIM) [25,26], and, more recently, also ISM [27] and RESCH [28], which is a specific form of eISM.

The following equation describes a multi-view variant of the Lucy Richardson algorithm [29,30], which is an iterative image reconstruction algorithm that maximizes the likelihood for a true estimate under the presence of Poisson noise. The algorithm estimates the object from a set of given 2D images $I_m(x_s, y_s)$ and their associated 3D PSFs $h_m(x, y, z)$ [23,28]:

$$E^{n+1}(\vec{x}) = E^n(\vec{x}) \cdot \left\{ \frac{1}{M} \sum_{m=1}^{M} \left[\left(\frac{V_m(\vec{x})}{E^n(\vec{x}) * h_m(\vec{x}) + \varepsilon} - 1 \right) * h_m(-\vec{x}) \right] + 1 \right\}. \tag{4}$$

Here, $E(\vec{x})$ is the 3D object estimate. The quantities V_m correspond to volume grids containing the measured images $I_m(x, y)$ in their center planes, and zeros elsewhere. M denotes the total number of detector pixels used. ϵ is a small constant to avoid singularities but should otherwise have negligible effect on the result. The initial estimate $E^0(\vec{x})$ can be filled with a constant value corresponding to the average intensity over all measurements I_m.

4. HELIX-HELIX PSF IMAGING

As was recently shown [17], capturing 3D information in a single 2D scan is possible if a pixelated detector is employed and the detection PSF suitably shaped. In this method, which we termed RESCH, an image is taken at every scanpoint and processed to retrieve depth information of the sample structure. The technique can also be combined with pixel reassignment [15] in order to improve the spatial resolution beyond that of a confocal microscope [28]. The achievable refocusing range in the particular system demonstrated, i.e., the z extension of the 2D-scanned region was about as large as the z resolution. For example, in a high numerical aperture (NA) system with a z resolution of 500 nm, the refocusing range was about ±250 nm.

The main limit for the refocusing range in the original RESCH implementation was the short axial length of the excitation focus, which was not altered and thus approximately Gaussian. Therefore, approaches for extending the refocusing range aim at stretching the excitation focus to a length comparable to that of the detection PSF. This can be achieved via several methods. One option is to reduce the NA on the excitation side. Since the axial length is reciprocally proportional to the square of the NA, this can be effective, but on the other hand also reduces the lateral resolution. Another option is to use PSFs with an increased depth of focus, such as a Bessel-like beam, which can be achieved by a ring-shaped transmission function in the objective pupil [31,32]. Alternatively, it is also possible to use helical PSFs in the excitation and emission paths. We identified this to be the best option among the listed possibilities because the resulting imaging system exhibits the best axial resolution. In effect, the helical PSF combines both a rapid axial variation while keeping a fairly constant (depth variant) cross section. This advantage has been confirmed in simulations (see Supplement 1).

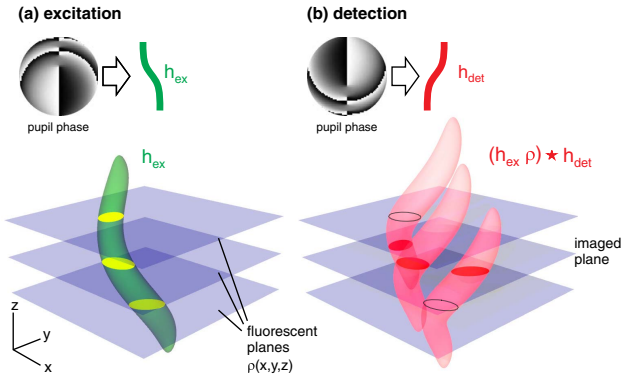

Fig. 2. Imaging of a three-layered fluorescent structure in the helix-helix system. (a) The helical excitation focus (green) is produced by a helical phase mask (greyscale image) and excites the layers at approximately elliptical intersection regions (yellow). (b) Another helical phase mask in the detection arm (greyscale image) forms the detection PSF into a helix as well. The plane that is finally imaged onto the camera is the center plane of $(h_{ex} \cdot \rho) \star h_{det}$. If the handedness of h_{det} (red helix) is different from h_{ex}, the images of the excited zones show a large lateral separation on the camera (red elliptic zones).

The excitation and detection pupil functions of a helix-helix system are shown in Fig. 2. Both masks produce helically shaped PSFs. The outline for the design algorithm of the phase masks is provided in [28] following [33,34]. Note that the helical phase masks in the excitation and detection pupils are identical except for a rotation of 180 deg. In order to understand the rationale of this design, it is helpful to consider the 3D illustrations in the figure, which are a graphical interpretation of the wide-field image formation equation [Eq. (1)] for the specific case of an object made of three thin fluorescent layers at a certain interspacing z_0: $\rho(\vec{x}) \propto \delta(z - z_0) + \delta(z) + \delta(z + z_0)$. The layers should have a sufficiently low extinction such that the attenuation of the excitation beam is negligible. Figure 2(a) depicts the excitation: the helical excitation focus (here represented by a green 3D iso-intensity surface) intersects the layers, exciting them at approximately elliptic intersection regions. Figure 2(b) is the graphical interpretation of Eq. (1) for $h_{det}(x, y, z) = h_{ex}(x, y, -z)$, i.e., an inverted handedness for the detection helix. The illustration shows that this is better than using the same handedness, because the images of the three excited regions appear maximally separated at the central plane, improving the z resolution of the final helix-helix system.

In order to realize $H_{det}(k_x, k_y, k_z) = H_{ex}(k_x, k_y, -k_z)$, we use phase masks $P_{ex}(x_{SLM}, y_{SLM})$ and $P_{det}(x_{SLM}, y_{SLM})$, where x_{SLM} and y_{SLM} are the physical real-space coordinates (typically on an SLM). Taking into account that the excitation and detection pupil spaces have inverted k_x, k_y, and k_z axes, we come to the conclusion that $P_{ex}(x_{SLM}, y_{SLM}) = P_{det}(-x_{SLM}, -y_{SLM})$, which corresponds to a rotation of 180 deg between the masks, which are shown in the insets of Fig. 2.

A. Imaging Properties of the Helix-Helix PSF System

We simulated the PSFs h_m for each pixel m of a detector featuring 15 × 15 pixels. Each detector pixel covers a size of $(\lambda/3)^2$ in the object space, and the NA is assumed to be 0.92 · RI, where RI is the refractive index of the specimen (this corresponds to a NA of 1.4 for an oil immersion objective).

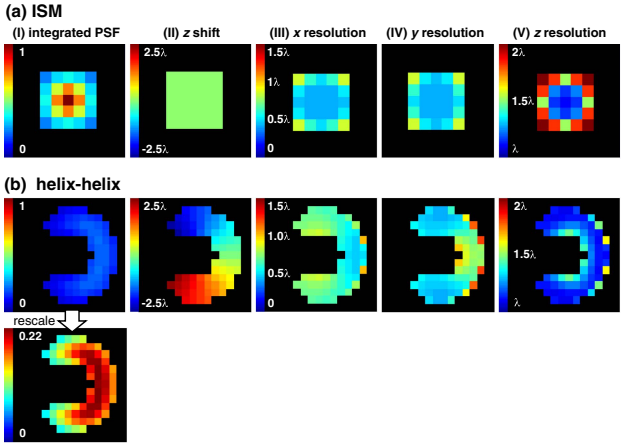

Fig. 3. Properties of 3D PSFs h_m in: (a) ISM and (b) helix-helix imaging. The PSF properties are color-coded in the five images (NA = $0.92 \cdot$ RI, with RI being the sample refractive index; circular excitation polarization and unpolarized fluorescence, but no Stokes shift assumed; λ is the wavelength in a medium with a refractive index RI).

Figure 3 depicts calculated properties of the PSFs h_m, for regular ISM as well as the helix-helix system. These plots enable rapid quantification and comparison of the imaging performance. Projections of these PSFs (and the PSFs of other imaging modes discussed later and in the supplementary document) are shown in Visualization 1, Visualization 2, Visualization 3, Visualization 4, and Visualization 5. Each of the square images in the figure represents the detector, and the colors of the respective pixels code one specific PSF property: (I) shows the integrated PSFs, which are a measure for the collected energy. For helix-helix imaging, two plots are shown: one sharing the scale with the respective ISM image and one (shown below) normalized to the respective maximum value in ISM. (II) Shows the z centroid positions of 3D Gaussian fits to h_m, and (III)–(V) show the full widths at half-maximum (FWHM) along all three axes of these Gaussian fits. The widths serve as estimate for the spatial resolution provided by h_m.

For ISM, properties of the 25 strongest PSFs (according to their maximum values) are shown. The corresponding pixels cover an area of 2 Airy discs. Reading out more pixels would predominantly provide additional low-frequency information of the object. It is noticeable that already the PSFs of the outer fringe pixels have significantly increased widths along all three axes. Figure 3(b) shows the 75 strongest PSFs for helix-helix imaging. In contrast to the ISM PSFs, they are all very compact along the z axis. Along $x - y$, however, they are broader than the ISM PSFs in some regions.

In view of the 3D imaging capability, we see that the z planes of the helix system cover a range of about $\pm 2.5\lambda$ without leaving gaps, where λ denotes the wavelength in the respective medium. The "refocusing range" is thus about four times larger than the z resolution (z-FWHM), which is about 1.2λ. The $x - y$ resolutions range from 0.44λ to about λ, depending on the z plane, which is about 1 to 2 times the value of ISM (0.43λ for the best PSFs). There is also a native anisotropy between the x and y resolutions, which originates from the approximately elliptic cross sections of the helical excitation and detection PSFs.

Next we investigate the light efficiency of helix-helix imaging in comparison with ISM. It is important to understand that both systems can in principle have the same light efficiency, since for both the camera collects the same fraction of generated signal photons if we neglect the small losses caused by the diffractive phase masks. However, significant efficiency differences are introduced by synthetic pinholing, i.e., by discarding the signal contained in certain detector pixels. In practice, discarding pixels is required if (a) the noise in the pixel dominates over the signal and including the pixel value would only decrease the SNR of the final image, and (b) high demands set by the scan speed make it necessary to restrict the number of pixels.

We would like to note that it is not necessary to choose a small synthetic pinhole (SP) in order to preserve the optical sectioning of the microscope as in optically implemented versions of ISM [35–38]. There, pixel reassignment is inherent to the system, and the total PSF is the sum of the shifted PSFs h_m. Therefore, pixels whose h_m are long-stretched in z will also stretch the total PSF and consequently degrade the optical sectioning. A *computational* ISM system such as eISM, however, stores the data collected by every detector and thus allows for more sophisticated ways of object reconstruction, such as the use of multi-view deconvolution algorithms [23,28], which take the shapes of all PSFs h_m into account and output the most likely estimate of the specimen, weighting their relative signal to noise.

For helix-helix imaging and ISM, Fig. 4 shows plots of the energies contained in the pixel-specific PSFs h_m as a function of the detector number (dashed lines). The detectors are listed in descending order according to their signal strength. Also shown is the total energy harvest, i.e., the light energy collected by all detector pixels up to the number given on the x axis (solid lines). The solid lines are thus cumulative sums of the dashed lines. The energy harvests are given in percent of the energy collected by a squared sensor of 16 Airy units (AU) side length (the value was motivated by the available computational power). The calculation further assumes an object thickness of 20 wavelengths, a NA of

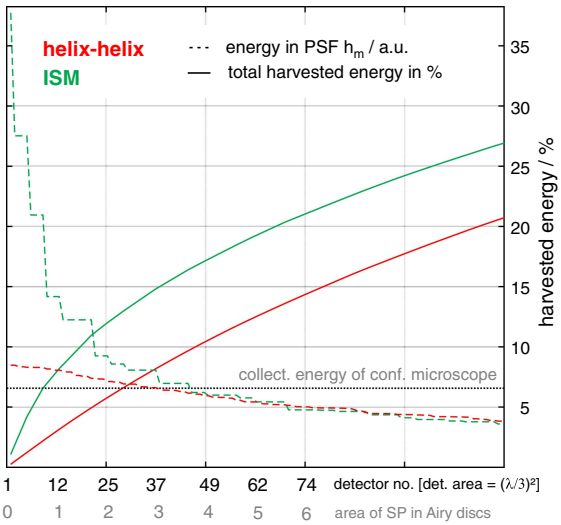

Fig. 4. Energy harvests for ISM (green plots) and helix-helix imaging. Dashed lines: energies contained in the pixel-specific PSFs h_m, in descending order. The detector number refers to the energy contained. Solid lines: cumulative sums of dashed lines, i.e., total energy harvest of all pixels up to the number on the x axis. The harvests for ISM and helix-helix imaging converge for very large detector areas (see extended graphs in Supplement 1). The energy harvest of a confocal microscope [pinhole diameter 1 Airy unit (AU)] is also marked with a horizontal gray line.

$0.92 \cdot \mathrm{RI}$, circular excitation polarization, unpolarized fluorescence, and no absorption of the excitation laser when passing through the object. The figure allows one to judge qualitatively how many detectors should be ideally read out for a given noise floor. For the respective strongest detectors, the ISM signal is about four to five times higher than for helix-helix imaging. One has to bear in mind, however, that about 4 z planes are simultaneously excited in the latter method with the same excitation laser power. One also sees that for achieving the same light collection efficiency, a larger SP has to be defined for helix-helix imaging. For instance, a SP with an area of about 3 Airy discs in helix-helix imaging collects the same amount of light as a confocal microscope with a pinhole area of 1 Airy disc.

The size of the SP is the product of effective pixel size (i.e., the size of the image of a detector pixel in the specimen plane) and the number of pixels that are read out. Different combinations between effective pixel size and number are possible for a given SP size (and thus light efficiency). Many small pixels are beneficial for the spatial resolution but imply a high data transfer rate, whereas a few large pixels produce less read-out noise and ease the data transfer at the cost of resolution. Simulations (see Supplement 1) show that choosing an effective pixel side length smaller than about 0.2 AU (equals about $\lambda/3$ for a NA of 1.4) provides almost no further resolution benefit. Therefore, a value of $\lambda/3$ is assumed in our simulations.

In practical imaging scenarios, if we assume a sufficiently thick specimen, the total photon efficiency of helix-helix imaging can be comparable to ISM. In particular, the efficiency of a confocal microscope with an Airy-disc-sized pinhole (corresponding to a pinhole area of $\pi/4$ Airy discs) can be easily met. For strongly scattering specimens, however, it is to be expected that crosstalk between the detector pixels reduces the image contrast and SNR.

5. GENERALIZED MULTIPLANE IMAGING USING EISM

The helix-helix microscope investigated in the previous section represents one particular design, which can be modified to trade refocusing range against SNR and resolution. In many situations, however, the transverse resolution of the helix-helix system will be inferior compared to ISM. A possible strategy to combine both 3D imaging and the high resolution of ISM is to engineer the excitation and detection PSFs using beam-splitting phase masks. In the excitation path, such masks can produce a number of laser foci whose 3D positions can be arbitrarily chosen within certain limits [39]. Such holographic multi-beam targeting is routinely used in holographic optical trapping [40] and has also been demonstrated for microscopy [41]. For the purpose of image scanning microscopy, however, where the signal is descanned and imaged onto a camera, this approach does also require to compensation with spot-dependent defocus values such that all generated fluorescence is sharply focused onto the camera. This can be facilitated by another beam-splitting phase mask in the detection path and has been demonstrated for wide-field microscopy [42,43]. The working principle of the beam-splitting method is outlined in Fig. 5, again using the example of a three-layered fluorescent structure. In this example, the excitation phase mask generates three equidistant foci along the optical axis, exciting the structure at circular cross sections. If read out with a collimated beam, the detection phase mask would likewise generate three spots with equal axial interspacing, however at varying lateral positions.

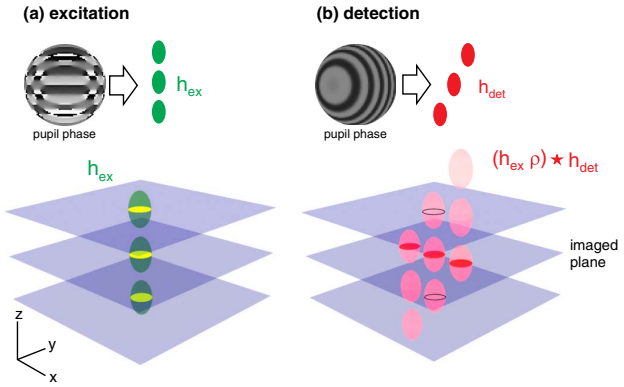

Fig. 5. Imaging of a three-layered fluorescent structure in beam-splitting eISM, designed to scan three z planes in parallel. (a) Three foci excite the layers at the circular intersection regions (yellow). (b) The plane recorded by the camera is the center plane of $(h_{\mathrm{ex}} \cdot \rho) \star h_{\mathrm{det}}$.

From the image formation described in Eq. (1) we conclude that nine foci are generated in total, three of which are positioned at the camera plane. The remaining six foci are in other z planes, which practically means that their light is lost if the focal distances to the camera are too large for the light to be recorded at a sufficient SNR. For this case, if n different planes are imaged in the detection path, a fraction of about $1/n$ is sharply imaged. In practice, it might be even slightly less, because the diffraction efficiency of the mask is lower than 100%. The same efficiency issue is known for wide-field multiplane imaging using beam-splitting phase diffractive masks. In contrast to wide-field microscopy, however, where large image fields have to be separated, and dispersion-compensating refractive optics are mandatory for broadband fluorescence [44], the spatial frequency content of beam-splitting phase masks in scanning microscopy is much lower because the lateral separation only needs to be on the order of a few Airy discs.

As an example for beam-splitting eISM, we would like to investigate parallel scanning at a NA of $0.92 \cdot \mathrm{RI}$ using three foci with a z interspacing of 1.5λ. We choose a focus arrangement that is different from the case illustrated in Fig. 5, which serves well from an educational point of view but is less suitable for an experiment, because such close-set foci would produce undesired crosstalk in a real sample. Therefore, we choose the three excitation foci to be sitting along a helical line with radius $R_0 = 1.5\lambda$, which spirals around the z axis. A 3D sketch of this focus distribution is provided in the Supplement 1. If we denote the 3D intensity distribution of an unmodified focus as $I_0(x, y, z)$, the excitation and detection PSFs are

$$\begin{aligned} h_{\mathrm{ex}} \propto\ & I_0(x - R_0 \sin(60°), y - R_0 \cos(60°) \\ & + I_0(x, y + R_0, z) +, z - \Delta z) \\ & + I_0(x + R_0 \sin(60°), y - R_0 \cos(60°), z + \Delta z) \\ h_{\mathrm{det}} \propto\ & I_0(x - R_0 \sin(60°), y - R_0 \cos(60°) - S_y, z - \Delta z) \\ & + I_0(x, y + R_0, z) \\ & + I_0(x + R_0 \sin(60°), y - R_0 \cos(60°) + S_y, z + \Delta z). \end{aligned} \quad (5)$$

Here, S_y denotes the separation of the foci on the camera chip. For $S_y = 0$, h_{ex} and h_{det} would be identical, and all foci would overlap. For our simulation example we choose $S_y = 1.5\lambda$.

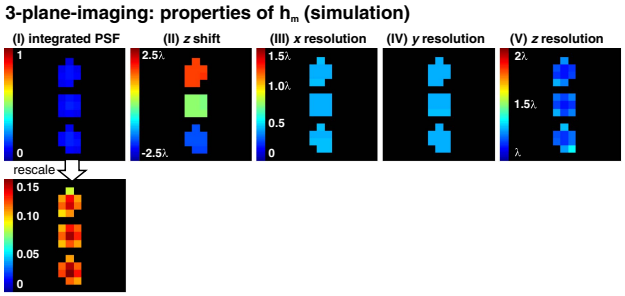

Fig. 6. Three-plane imaging: simulated properties of the 27 strongest 3D PSFs h_m (NA $= 0.92 \cdot$ RI).

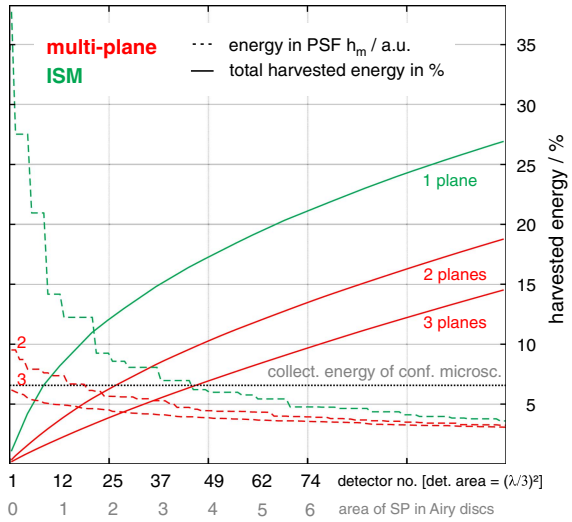

Fig. 7. Energy harvests for ISM (green plots) and beam-splitting eISM for the imaging of two and three planes, respectively. Dashed lines: energies contained in PSFs h_m. Solid lines: cumulative energy collected by all PSFs up to number given on the x axis.

Figure 6 shows the detector pixels with properties of their PSFs h_m. The integrated PSF intensities shown in the second row image are again normalized to the respective maximum values of regular ISM. The simulated data shows that the PSF widths along all three axes are comparable to ISM. In contrast to the helix-helix approach, three distinct planes are scanned rather than a continuous volume. In our example, the light collected by the 27 strongest detectors is about a third compared to ISM with 25 detectors. The simulated z shifts are exactly at $\pm 1.5\lambda$, as designed.

Figure 7 shows the energies in the detector-specific PSFs h_m as well as the total energy harvests for ISM, two- and three-plane imaging, respectively. The three-plane imaging PSFs are the ones described by Eq. (5), whose properties are shown in Fig. 6. For two-plane imaging, we simulated the use of binary beam splitters to obtain simultaneous scanning of the planes at $z = \pm 1.5\lambda$ (see Supplement 1). While binary patterns ensure equally intense diffraction orders, they have a low diffraction efficiency of only 81% (40.5% in the first and minus first orders) compared to the 1-to-3 beam-splitting masks (efficiency >90%). This explains the relative poor performance of the 2-plane imaging mode compared to ISM and 3-plane imaging.

6. EXPERIMENTAL RESULTS

Figure 8 shows experimental results from imaging stained mitochondria in COS 7 cells (Alexa 647, NA 1.4).

The boxes on top show a confocal image and a ISM image taken at about $z = +0.25$ μm (a slight focus drift caused the offset from the target plane $z = 0$). An unprocessed wide-field image

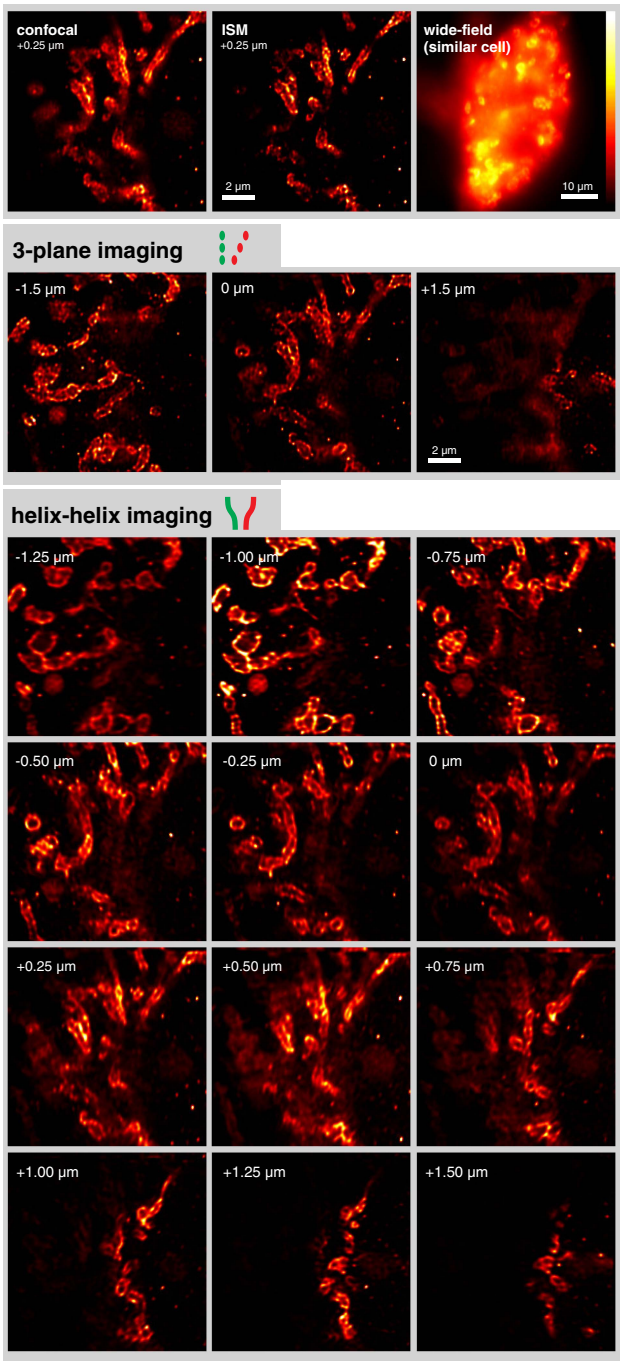

Fig. 8. Three-plane versus helix-helix imaging (NA 1.4) of a COS 7 cell with Alexa647-stained mitochondria. Upper box: confocal (pinhole diam. 0.8 AU), ISM, and wide-field images, Middle box: the three images are obtained in a single scan using beam-splitting phase masks (81 views were jointly deconvolved using 75 iterations). The numbers in the images indicate their z position. Lower box: helix-helix image series of the same cell (114 views jointly deconvolved in 200 iterations).

of a similar cell is shown as well, to provide a better impression of the sample properties (e.g., scattering). The ISM image was deblurred using 50 iterations of a multi-view Lucy Richardson algorithm [Eq. (4)] using measured PSFs. More iterations visibly degraded the image quality. The confocal image was constructed from the same ISM data set by adding all "single-pixel" confocal images and deblurring the result in 25 iterations using a single PSF, which was the sum of all ISM PSFs. The effective pinhole diameter for the confocal image was 0.8 AU.

The box in the middle shows three images obtained with beam-splitting eISM at the chosen z coordinates of $+1.5$ μm, 0 μm, and -1.5 μm. The laser power for the three-plane scan was, with 20 μW (measured before the objective), about three times higher than the ISM scan power. The pixel dwell time was 2.5 ms (determined by the camera speed). 200×200 scanpoints were recorded during the scan, covering an area of 16×16 μm^2. Compared with the ISM image, the three-plane-scan provides images of similar spatial resolution. The result was obtained by jointly deblurring 81 single-pixel confocal images ("views") using 75 iterations. All deconvolution operations were performed using measured PSFs.

The lower box contains a series of z planes resulting from a helix-helix scan. The planes cover a range of almost 3 μm. The used laser power was, with 13 μW, only twice as high as for the ISM scan. Other imaging parameters such as pixel dwell time are the same as for the three-plane scan. As expected, the spatial resolution is lower compared to ISM or the three-plane-scan; however, the volume information provided is continuous over the covered z range. This continuity allows for deblurring the entire dataset (114 "single-pixel" confocal images) in a single 3D deconvolution step (200 iterations), which leads to a higher optical sectioning in the final images. This is especially noticeable when comparing the $+1.5$ μm images of the three-plane and helix-helix scans. On the other hand, if we compare the ISM image with the respective helix-helix section at $z = +0.25$ μm, it seems that the sectioning of ISM was superior. A possible reason for this observation is the already mentioned crosstalk, i.e., scattered light that ends up being detected by "wrong" pixels.

In this case, i.e., for deconvolving images of 200×200 pixels size and 114 views, the deconvolution algorithm took about 16 s per iteration, using an Intel Xeon(R) CPU E5-1620 at 3.6 GHz with 8GB RAM. Significant acceleration of the algorithm would be possible using GPU-assisted computing.

Another experimental result obtained with helix-helix imaging is shown in Fig. 9. The sample is a distribution of fluorescent microbeads ("PS speck" beads of Molecular Probes, 175 nm diameter, dye: "deep red"), which were air-dried on a glass cover slip and mixed into a small drop of curing mounting medium (ProLong Diamond antifade mountant of ThermoFisher Scientific). The figure also shows ISM images of the same sample volume as the control measurement. While the helix-helix PSF acquires the entire volume of almost 3 μm thickness in a single $x-y$ scan, we had to take several ISM images in sequence with intermediate z stepping in order to reconstruct the same volume.

The pixel dwell times for all scans performed in this experiment are 2.5 ms. The helix-helix data set consisted of 158 views and was deconvolved using 300 iterations. We found that using significantly more iterations tended to introduce visible artifacts. A z stack built from eleven separate ISM scans (21 views used per scan), taken at 300 nm z interspacings, was deconvolved using

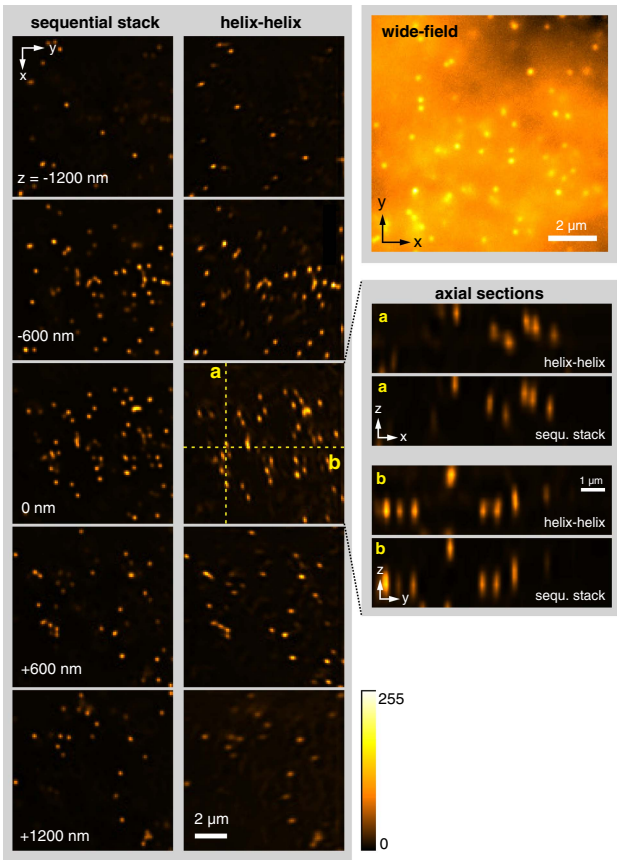

Fig. 9. Helix-helix images of a 3D distribution of fluorescent microbeads (NA 1.25, wavelengths: ex./em. = 640/660 nm, refractive index of mounting medium = 1.47). The two image columns on the left show different $x-y$ sections of the helix-helix image data and a sequentially taken ISM stack for comparison. The corresponding z values are stated in the images. The four rectangular images at the right show two axial cross sections (a and b) through both stacks. Their positions in the sample volume are indicated by the yellow dashed lines. The image at the upper right corner shows an exemplary wide-field image of the sample. The color scale bar applies to all images. Both the helix-helix and ISM stacks have been normalized to 255.

100 iterations. All deconvolution operations were performed using measured PSFs.

The two image columns in the figure again demonstrate the 3D imaging capability of the helix-helix modality: all beads are accurately reconstructed at their true positions. It is also visible that the $x-y$ resolution of ISM is superior to the helix-helix system, despite the fact that many more deblurring iterations were used on the helix-helix data. Also, the $x-y$ resolution anisotropy is perceptible in the helix-helix images.

7. DISCUSSION AND OUTLOOK

We presented an image scanning microscope with freely programmable excitation and detection pupil functions. Using this general platform of engineered PSF ISM, we investigated two schemes for 3D imaging. The first employs helical PSFs in both paths and allows one to capture continuous sample information along the z axis. The z range obtained is about four times larger than the z resolution according to Rayleigh. The axial resolution is equal to

(image-recording) ISM and thus slightly better than that of a standard confocal microscope. The lateral resolution was found to be z-dependent and anisotropic. The lateral PSF widths are up to twice as wide as in ISM. Helix-helix imaging might prove less practical for strongly scattering samples, such as brain tissue, because of crosstalk between adjacent detectors.

The proposed beam-splitting method, however, can avoid crosstalk by choosing large enough focus separations. This scheme employs beam-splitting phase masks in the excitation and detection pupils, thus enabling the simultaneous scanning of multiple discrete planes at the 3D resolution of ISM. As the light efficiency roughly drops as one over the number of imaged planes, we anticipate that the method is feasible for a limited number of planes. The plane positions can be freely chosen within limits set by dispersion and the spatial resolution of the pupil masks [39]. While dispersion is usually not a problem on the excitation side, it plays a role for the detection due to the fluorescence bandwidth: the pupil masks are basically a superposition of diffractive lenses, whose refractive powers are proportional to the wavelength. Thus, a wavelength shift of 10% causes a z-plane shift of likewise 10% for the detection.

The two scanning schemes presented in this paper are examples that demonstrate the possibilities and limits of PSF engineering in ISM in view of 3D imaging. They may not necessarily represent optimal strategies, as such an attribute requires an *a priori* definition of "optimal" and thus depends on the individual imaging application. A practical route to find optimal PSF shapes for a particular situation would be to distill certain figures of merit from a given imaging task, such as SNR, 3D resolution, or z range. Based on these figures, an optimal PSF shape could be found by employing optimization routines. Similar strategies for PSF design have been used before [45–49]. Optimal design algorithms could also include prior knowledge matched to a specific task.

The potential of ISM-based 3D imaging as presented in this work lies in the possibility to scan volumes at high speeds without the requirement to refocus in between scans. This can be advantageous for numerous imaging applications, such as microscopy and profilometry, although the latter application requires the data processing to be adapted to coherent image formation [15]. Sample information along the z axis can be captured truly simultaneously at an axial resolution that equals that of ISM, provided the detector pixels are simultaneously read out. This stands in contrast to alternative fast scanning methods, such as spinning disc microscopy, where scanning a 2D plane is fast, but there is a need to mechanically step to other focus points.

However, we point out that obtaining a significant speed advantage over traditional scanning systems will require a different detector than the sCMOS camera used in this proof-of-concept system, for instance a single photon avalanche diode (SPAD) array (as for instance used in ISM by Castello *et al.* [50]) or a multichannel photo-multiplier tube (PMT) (such as implemented in the commercial ISM version of Zeiss [51]). Although the high data throughput provided by sCMOS cameras can be utilized using parallelized excitation, the fact that 3D information is mapped onto a 2D sensor would require increasing the spacing in between excitation helices, thus mitigating the speed advantage.

In view of 3D imaging capabilities, optical scanning holography (OSH) [52] represents a somewhat related imaging approach which—even though mainly used for coherent imaging—is also compatible with fluorescence microscopy [53]. Although the applications are similar, the functional principles of eISM for 3D imaging and OSH are quite different. The former method relies on engineering excitation and detection pupils and detects intensity with a pixelated detector, while the latter method is a holographic technique that excites with a temporarily changing interference pattern and heterodyne intensity detection. The phase-sensitive detection facilitates holographic 3D reconstruction of objects using numerical backpropagation, while the 3D information collected in eISM is processed using a maximum-likelihood algorithm.

This paper focuses on 3D imaging strategies that rely on the generalized pupil engineering possibilities of eISM. However, the concept offers further possibilities beyond volumetric imaging, as for instance the efficient collection of spectroscopic information or polarization information (potentially revealing the orientation of molecules), or information about aberrations introduced by the system or specimen. A straightforward approach for multicolored spectroscopic imaging, for example, would be to use a programmed grating in the excitation pupil in order to simultaneously focus lasers of different wavelengths to closely spaced excitation sites and another grating in the detection pupil to investigate the spectra of the excited fluorescence. Likewise, efficient measurements of dipole orientations could be facilitated by shaping the excitation polarization state (e.g., such as described in [54,55]) for optimal excitation, combined with polarization-sensitive detection (as has been demonstrated for wide-field microscopy [56–58]). In view of aberration correction, the introduced eISM platform allows for separate wavefront corrections on the excitation and emission sides, which can be useful for descanned two-photon or harmonic generation microscopy where the wavelengths (and thus aberrations) on the excitation and detection sides are different. Additionally, aberration measurements based on indirect wavefront sensing [59], which is robust but requires several subsequently performed test scans, could be parallelized and thus made faster. In general, the equal importance of excitation and detection PSFs in scanning systems means that eISM has the potential to outperform alternative PSF engineering approaches, exclusively altering either the excitation or the detection PSF.

Funding. Austrian Science Fund (FWF) (P 30214-N36); National Science Foundation (NSF) (1548924, 1556473).

Acknowledgment. The authors thank Martin Offterdinger for providing the biological specimens.

See Supplement 1 for supporting content.

REFERENCES

1. S. W. Hell and J. Wichmann, "Breaking the diffraction resolution limit by stimulated emission: stimulated-emission-depletion fluorescence microscopy," Opt. Lett. **19**, 780–782 (1994).
2. G. T. di Francia, "Nuovo pupille superresolventi," Atti Fond. Giorgio Ronchi **7**, 366–372 (1952).
3. Z. Hegedus and V. Sarafis, "Superresolving filters in confocally scanned imaging systems," J. Opt. Soc. Am. A **3**, 1892–1896 (1986).
4. M. Martínez-Corral, M. T. Caballero, E. H. K. Stelzer, and J. Swoger, "Tailoring the axial shape of the point spread function using the Toraldo concept," Opt. Express **10**, 98–103 (2002).
5. H. P. Kao and A. S. Verkman, "Tracking of single fluorescent particles in three dimensions: use of cylindrical optics to encode particle position," Biophys. J. **67**, 1291–1300 (1994).

6. R. P. Pavani and R. Piestun, "Three dimensional tracking of fluorescent microparticles using a photon-limited double-helix response system," Opt. Express **16**, 22048–22057 (2008).
7. E. R. Dowski and W. T. Cathey, "Single-lens single-image incoherent passive-ranging systems," Appl. Opt. **33**, 6762–6773 (1994).
8. J. Campos, J. C. Escalera, C. J. Sheppard, and M. J. Yzuel, "Axially invariant pupil filters," J. Mod. Opt. **47**, 57–68 (2000).
9. A. Greengard, Y. Y. Schechner, and R. Piestun, "Depth from rotating point spread functions," Proc. SPIE **5557**, 91–97 (2004).
10. E. J. Botcherby, R. Juškaitis, and T. Wilson, "Scanning two photon fluorescence microscopy with extended depth of field," Opt. Commun. **268**, 253–260 (2006).
11. C. J. R. Sheppard and A. Choudhury, "Image formation in the scanning microscope," J. Mod. Opt. **24**, 1051–1073 (1977).
12. Z. S. Hegedus, "Annular pupil arrays," J. Mod. Opt. **32**, 815–826 (1985).
13. M. Martínez-Corral, P. Andres, J. Ojeda-Castaneda, and G. Saavedra, "Tunable axial superresolution by annular binary filters. Application to confocal microscopy," Opt. Commun. **119**, 491–498 (1995).
14. A. Jesacher, S. Bernet, and M. Ritsch-Marte, "Colored point spread function engineering for parallel confocal microscopy," Opt. Express **24**, 27395–27402 (2016).
15. C. J. R. Sheppard, "Super-resolution in confocal imaging," Optik **80**, 53–54 (1988).
16. C. Müller and J. Enderlein, "Image scanning microscopy," Phys. Rev. Lett. **104**, 198101 (2010).
17. A. Jesacher, M. Ritsch-Marte, and R. Piestun, "Three-dimensional information from two-dimensional scans: a scanning microscope with post acquisition refocusing capability," Optica **2**, 210–213 (2015).
18. C. W. McCutchen, "Generalized aperture and the three-dimensional diffraction image," J. Opt. Soc. Am. **54**, 240–244 (1964).
19. C. J. R. Sheppard, S. B. Mehta, and R. Heintzmann, "Superresolution by image scanning microscopy using pixel reassignment," Opt. Lett. **38**, 2889–2892 (2013).
20. A. P. Dempster, N. M. Laird, and D. B. Rubin, "Maximum likelihood from incomplete data via the EM algorithm," Journal of the Royal Statistical Society Series B **39**, 1–38 (1977).
21. R. E. Blahut, *Theory of Remote Image Formation* (Cambridge University, 2004).
22. L. A. Shepp and Y. Vardi, "Maximum likelihood reconstruction for emission tomography," IEEE Trans. Med. Imaging **1**, 113–122 (1982).
23. R. Heintzmann, G. Kreth, and C. Cremer, "Reconstruction of axial tomographic high resolution data from confocal fluorescence microscopy: a method for improving 3D FISH images," Anal. Cell. Pathol. **20**, 7–15 (2000).
24. R. Heintzmann, Q. Hanley, D. Arndt-Jovin, and T. Jovin, "A dual path programmable array microscope (PAM): simultaneous acquisition of conjugate and non-conjugate images," J. Microsc. **204**, 119–135 (2001).
25. U. Krzic, "Multiple-view microscopy with light-sheet based fluorescence microscope," Ph.D. dissertation (European Molecular Biology Laboratory (EMBL), 2009).
26. M. Temerinac-Ott, O. Ronneberger, P. Ochs, W. Driever, T. Brox, and H. Burkhardt, "Multiview deblurring for 3-D images from light-sheet-based fluorescence microscopy," IEEE Trans. on Image Process. **21**, 1863–1873 (2012).
27. M. Ingaramo, A. G. York, E. Hoogendoorn, M. Postma, H. Shroff, and G. H. Patterson, "Richardson-Lucy deconvolution as a general tool for combining images with complementary strengths," Chem. Phys. Chem. **15**, 794–800 (2014).
28. C. Roider, R. Heintzmann, R. Piestun, and A. Jesacher, "Deconvolution approach for 3D scanning microscopy with helical phase engineering," Opt. Express **24**, 15456–15467 (2016).
29. W. H. Richardson, "Bayesian-based iterative method of image restoration," J. Opt. Soc. Am. **62**, 55–59 (1972).
30. L. B. Lucy, "An iterative technique for the rectification of observed distributions," Astron. J. **79**, 745–754 (1974).
31. W. T. Welford, "Use of annular apertures to increase focal depth," J. Opt. Soc. Am. **50**, 749–759 (1960).
32. C. J. R. Sheppard and T. Wilson, "Imaging properties of annular lenses," Appl. Opt. **18**, 3764–3769 (1979).
33. R. Piestun and J. Shamir, "Control of wave-front propagation with diffractive elements," Opt. Lett. **19**, 771–773 (1994).
34. S. R. P. Pavani and R. Piestun, "High-efficiency rotating point spread functions," Opt. Express **16**, 3484–3489 (2008).
35. S. Roth, C. J. R. Sheppard, K. Wicker, and R. Heintzmann, "Optical photon reassignment microscopy," Opt. Nanoscopy **2**, 5 (2013).
36. A. G. York, P. Chandris, D. Dalle Nogare, J. Head, P. Wawrzusin, R. S. Fischer, A. Chitnis, and H. Shroff, "Instant super-resolution imaging in live cells and embryos via analog image processing," Nat. Methods **10**, 1122–1126 (2013).
37. G. M. R. De Luca, R. M. P. Breedijk, R. A. J. Brandt, C. H. C. Zeelenberg, B. E. de Jong, W. Timmermans, L. N. Azar, R. A. Hoebe, S. Stallinga, and E. M. M. Manders, "Re-scan confocal microscopy: scanning twice for better resolution," Biomed. Opt. Express **4**, 2644–2656 (2013).
38. T. Azuma and T. Kei, "Super-resolution spinning-disk confocal microscopy using optical photon reassignment," Opt. Express **23**, 15003–15011 (2015).
39. A. Jesacher, C. Roider, and M. Ritsch-Marte, "Enhancing diffractive multi-plane microscopy using colored illumination," Opt. Express **21**, 11150–11161 (2013).
40. G. C. Spalding, J. Courtial, and R. Di Leonardo, *Holographic Optical Tweezers* (Academic, 2008).
41. V. Nikolenko, B. O. Watson, R. Araya, A. Woodruff, D. S. Peterka, and R. Yuste, "SLM Microscopy: scanless two-photon imaging and photostimulation using spatial light modulators," Front. Neural Circuits **2** (2008).
42. P. M. Blanchard and A. H. Greenaway, "Simultaneous multiplane imaging with a distorted diffraction grating," Appl. Opt. **38**, 6692–6699 (1999).
43. C. Maurer, S. Khan, S. Fassl, S. Bernet, and M. Ritsch-Marte, "Depth of field multiplexing in microscopy," Opt. Express **18**, 3023–3034 (2010).
44. S. Abrahamsson, J. Chen, B. Hajj, S. Stallinga, A. Y. Katsov, J. Wisniewski, G. Mizuguchi, P. Soule, F. Mueller, C. D. Darzacq, X. Darzacq, C. Wu, C. I. Bargmann, D. A. Agard, M. Dahan, and M. G. L. Gustafsson, "Fast multicolor 3D imaging using aberration-corrected multifocus microscopy," Nat. Methods **10**, 60–63 (2013).
45. M. A. A. Neil, R. Juškaitis, T. Wilson, Z. J. Laczik, and V. Sarafis, "Optimized pupil-plane filters for confocal microscope point-spread function engineering," Opt. Lett. **25**, 245–247 (2000).
46. R. Piestun and J. Shamir, "Synthesis of 3D light fields and applications," Proc. IEEE **90**, 222–244 (2002).
47. G. Grover, S. R. P. Pavani, and R. Piestun, "Performance limits on three-dimensional particle localization in photon-limited microscopy," Opt. Lett. **35**, 3306–3308 (2010).
48. R. Piestun, C. J. Cogswell, A. D. Greengard, and Y. Y. Schechner, "Method and system for optical imaging and ranging," U.S. patent 7,705,970 (April 27, 2010).
49. Y. Shechtman, S. J. Sahl, A. S. Backer, and W. E. Moerner, "Optimal point spread function design for 3D imaging," Phys. Rev. Lett. **113**, 133902 (2014).
50. M. Castello, G. Tortarolo, M. Buttafava, A. Tosi, C. Sheppard, A. Diaspro, and G. Vicidomini, "Image scanning microscopy using a SPAD detector array (Conference Presentation)," Proc. SPIE **10071**, 1007101 (2017).
51. J. Huff, W. Bathe, R. Netz, T. Anhut, and K. Weisshart, "The Airyscan detector from ZEISS: confocal imaging with improved signal-to-noise ratio and super-resolution," Nat. Methods **12**, 1–19 (2015).
52. T. C. Poon, "Scanning holography and two-dimensional image processing by acousto-optic two-pupil synthesis," J. Opt. Soc. Am. A **2**, 521–527 (1985).
53. G. Indebetouw and W. Zhong, "Scanning holographic microscopy of three-dimensional fluorescent specimens," J. Opt. Soc. Am. A **23**, 1699–1707 (2006).
54. C. Maurer, A. Jesacher, S. Fürhapter, S. Bernet, and M. Ritsch-Marte, "Tailoring of arbitrary optical vector beams," New J. Phys. **9**, 78 (2007).
55. J. H. Clegg and M. A. A. Neil, "Double pass, common path method for arbitrary polarization control using a ferroelectric liquid crystal spatial light modulator," Opt. Lett. **38**, 1043–1045 (2013).
56. S. R. P. Pavani, J. G. DeLuca, and R. Piestun, "Polarization sensitive, three-dimensional, single-molecule imaging of cells with a double-helix system," Opt. Express **17**, 19644–19655 (2009).
57. M. P. Backlund, M. D. Lew, A. S. Backer, S. J. Sahl, G. Grover, A. Agrawal, R. Piestun, and W. E. Moerner, "Simultaneous, accurate measurement of the 3D position and orientation of single molecules," Proc. Natl. Acad. Sci. USA **109**, 19087–19092 (2012).
58. A. Agrawal, S. Quirin, G. Grover, and R. Piestun, "Limits of 3D dipole localization and orientation estimation for single-molecule imaging: towards Green's tensor engineering," Opt. Express **20**, 26667–26680 (2012).
59. M. J. Booth, "Adaptive optics in microscopy," Philos. Trans. R. Soc. A **365**, 2829–2843 (2007).